Title

Elucidating the mechanism of MgB 2 initial hydrogenation via a combined experimental—theoretical study

Journal

Physical Chemistry Chemical Physics, 19(34)

ISSN

0956-5000

Authors

Ray, Keith G

Klebanoff, Leonard E

Lee, Jonathan RI

et al.

Publication Date

2017-08-30

DOI

10.1039/c7cp03709k

Peer reviewed

Volume 19 | Number 34 | 14 September 2017 | Pages 22599–23542

PCCP

Physical Chemistry Chemical Physics

rsc.li/pccp

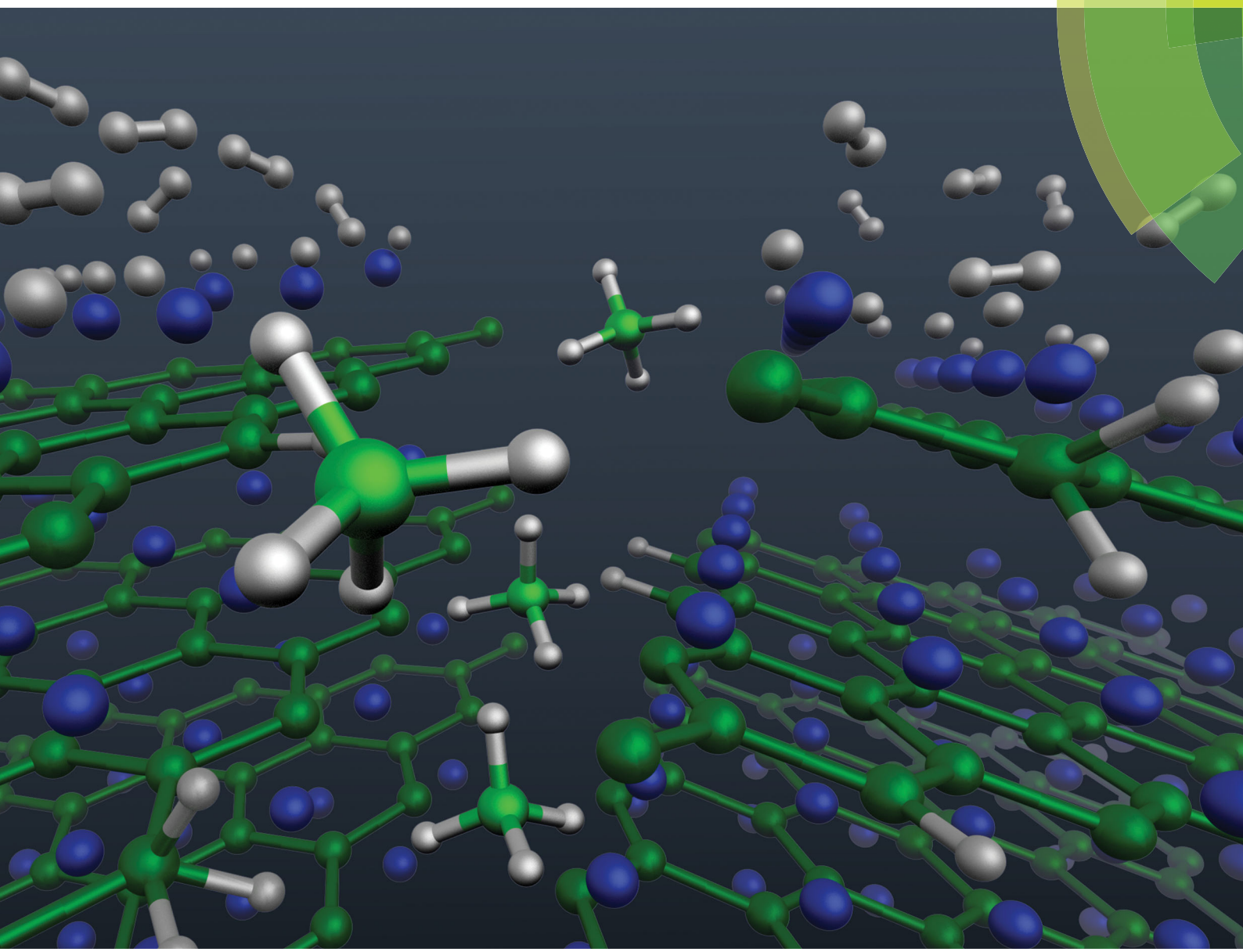

ISSN 1463-9076

ROYAL SOCIETY OF CHEMISTRY

PAPER

Leonard E. Klebanoff *et al.*

Elucidating the mechanism of MgB_2 initial hydrogenation *via* a combined experimental–theoretical study

PCCP

PAPER

View Article Online
View Journal | View Issue

Cite this: *Phys. Chem. Chem. Phys.*, 2017, **19**, 22646

Elucidating the mechanism of MgB_2 initial hydrogenation *via* a combined experimental–theoretical study†

Keith G. Ray,[a] Leonard E. Klebanoff,*[b] Jonathan R. I. Lee,[a] Vitalie Stavila,[b] Tae Wook Heo,[a] Patrick Shea,[a] Alexander A. Baker,[a] Shinyoung Kang,[a] Michael Bagge-Hansen,[a] Yi-Sheng Liu,[c] James L. White[b] and Brandon C. Wood[a]

Received 1st June 2017,
Accepted 19th July 2017

DOI: 10.1039/c7cp03709k

rsc.li/pccp

$Mg(BH_4)_2$ is a promising solid-state hydrogen storage material, releasing 14.9 wt% hydrogen upon conversion to MgB_2. Although several dehydrogenation pathways have been proposed, the hydrogenation process is less well understood. Here, we present a joint experimental–theoretical study that elucidates the key atomistic mechanisms associated with the initial stages of hydrogen uptake within MgB_2. Fourier transform infrared, X-ray absorption, and X-ray emission spectroscopies are integrated with spectroscopic simulations to show that hydrogenation can initially proceed *via* direct conversion of MgB_2 to $Mg(BH_4)_2$ complexes. The associated energy landscape is mapped by combining *ab initio* calculations with barriers extracted from the experimental uptake curves, from which a kinetic model is constructed. The results from the kinetic model suggest that initial hydrogenation takes place *via* a multi-step process: molecular H_2 dissociation, likely at Mg-terminated MgB_2 surfaces, is followed by migration of atomic hydrogen to defective boron sites, where the formation of stable B–H bonds ultimately leads to the direct creation of $Mg(BH_4)_2$ complexes without persistent B_xH_y intermediates. Implications for understanding the chemical, structural, and electronic changes upon hydrogenation of MgB_2 are discussed.

1 Introduction

The mitigation of global climate change in the face of increasing worldwide energy demand requires the swift adoption of a variety of zero-carbon renewable energy infrastructure and technologies. Transportation accounts for a large percentage of total greenhouse gas (GHG) emissions and utilizing carbon neutral renewables in this sector presents a unique set of challenges. Hydrogen-based power has great potential for addressing the need for zero-emission transportation technologies.[1] In fact, proton exchange membrane (PEM) fuel cell systems are already used in automotive and portable power applications as hydrogen energy conversion devices.[2]

The current generation of fuel cell light duty vehicles uses high-pressure (700 bar) "composite over-wrapped pressure vessels" (*i.e.* composite tanks) to store the hydrogen fuel. While enabling the roll-out of light duty fuel cell vehicles, 700 bar composite tanks are not optimal and alternative hydrogen storage systems/materials/approaches can, in principle, provide significantly improved gravimetric and volumetric hydrogen storage densities. Metal hydrides and other solid-state materials offer potential advantages for hydrogen storage, such as higher gravimetric and volumetric storage densities, filling from lower pressure hydrogen sources (thus avoiding compression energy losses), and added safety stemming from a typical order of magnitude lower overall hydrogen storage system pressure. However, metal hydrides that possess the high gravimetric and volumetric storage densities have not demonstrated adequate cyclability and fast refueling under practical conditions. To identify the causes of these limitations and strategies to mitigate them, better microscopic characterization of these materials during hydrogenation and dehydrogenation must be carried out.

The U.S. Department of Energy (DOE) has historically supported research in solid-state hydrogen storage materials, including complex metal hydrides,[3] and has established practical targets for hydrogen storage systems in light-duty vehicles. 700 bar storage of hydrogen does not satisfy all the DOE hydrogen storage benchmarks, but there is hope that solid-state hydrogen storage will

[a] *Lawrence Livermore National Laboratory, Livermore, California, USA*
[b] *Sandia National Laboratories, Livermore, California, USA.*
E-mail: lekleba@sandia.gov
[c] *Lawrence Berkeley National Laboratory, Berkeley, California, USA*

† Electronic supplementary information (ESI) available: Depth sensitivity of our spectroscopic methods; XRD patterns; additional FTIR spectra; simulated XAS and electronic DOS; kinetic model information. See DOI: 10.1039/c7cp03709k

allow all the DOE targets to be met and improve the driving range of light-duty fuel cell vehicles. According to recommendations from the DOE Metal Hydride Center of Excellence,[4] as well as a report by Pasini *et al.*,[5] magnesium borohydride ($Mg(BH_4)_2$) is one of the very few metal hydride candidates that lie close to the ''viability window'' of gravimetric capacity and desorption enthalpy (ΔH_{des}) required to satisfy the 2017 DOE storage targets. It has a high theoretical capacity of 14.9 wt% H derived from the overall dehydrogenation reaction: $Mg(BH_4)_2 \rightarrow MgB_2 + 4H_2$. Furthermore, the material has a volumetric hydrogen storage density of 117 g H_2 per L and can be cycled reversibly, although the temperatures and H_2 pressure currently required for rehydrogenation are too high. Like many solid-state complex hydride hydrogen storage systems, the $Mg(BH_4)_2/MgB_2$ system suffers from poor kinetics whose origin is not well understood. If the kinetic limitations could be removed and the effective ΔH_{des} slightly improved, then facile hydrogen uptake and release could be attained, and a $Mg(BH_4)_2$-based hydrogen storage system could meet all long-term DOE targets. To effect an improvement in the absorption enthalpy and kinetics, the detailed chemical and structural evolution during hydrogen cycling must first be identified. Thorough investigation of the material during hydrogenation would provide information on undesirable intermediates, for which formation may be suppressed, as well as the interfaces, surfaces, and defect structures important for the primary reaction, allowing for their optimization.

Virtually all prior studies of the $Mg(BH_4)_2/MgB_2$ system have focused on the dehydrogenation of $Mg(BH_4)_2$. In the original work reported by Konoplev and Bakulina,[6] it was proposed that decomposition followed the direct path: $Mg(BH_4)_2 \rightarrow MgH_2 + 2B + 3H_2$. This decomposition pathway was also assumed in the work of Nakamori *et al.*[7] Chlopek and co-workers[8] adopted a three-step dehydrogenation scheme connecting $Mg(BH_4)_2$ to MgB_2: $Mg(BH_4)_2 \rightarrow MgH_2 + 2B + 3H_2 \rightarrow Mg + 2B + 4H_2 \rightarrow MgB_2 + 4H_2$. The formation of MgB_2 implies the full release of 14.9 wt% H from the original $Mg(BH_4)_2$ material. Soloveichik *et al.*[9] revealed for the first time the existence of partially hydrogenated B–H reaction intermediates such as $MgB_{12}H_{12}$ during the dehydrogenation, which was accounted for theoretically by Ozolins and co-workers[10] and confirmed experimentally by Li *et al.*[11] Studies of $Mg(BH_4)_2$ decomposition for modest temperatures under varying background pressures of hydrogen report the additional formation of MgB_2H_7 and MgB_2H_6 along the dehydrogenation pathway.[12]

More recently, there has been work investigating the initial dehydrogenation step at modest temperatures[13,14] and at varying hydrogen back pressures.[15] Chong *et al.* reported[13] that dehydriding $Mg(BH_4)_2$ at 200 °C involves the formation of meta-stable magnesium triborane, $Mg(B_3H_8)_2$. At higher temperatures, $Mg(B_3H_8)_2$ is thought to decompose to form $MgB_{10}H_{10}$, $MgB_{12}H_{12}$, and other species.[13] Zhang *et al.*[16] have investigated theoretically the thermodynamics of the $Mg(BH_4)_2$ dehydrogenation pathway, assessing the energy of prospective intermediates such as $Mg(B_3H_8)_2$, MgB_3H_7, $Mg_3(B_3H_6)_2$, $Mg(B_2H_7)_2$, MgB_nH_n (n = 6, 7, 8, 9, 10, 11), and $Mg(B_{11}H_{14})_2$.

By comparison, very little work has been conducted for the rehydrogenation of MgB_2 and the intermediates (if any) that could be involved. Severa *et al.*[17] were able to directly hydrogenate MgB_2 to $Mg(BH_4)_2$ at 950 bar and 400 °C over 108 hours, and Pistidda *et al.*[18] produced $Mg(BH_4)_2$ directly by ball milling MgB_2 in hydrogen at 100 bar, in both cases apparently without appreciable $MgB_{12}H_{12}$ production. Newhouse *et al.* also demonstrated efficient conversion of MgB_2 into $Mg(BH_4)_2$ under 900 bar H_2 at 390 °C for 72 hours[19] and Li *et al.* reported the generation and hydrogenation of nanostructured MgB_2 with mechanical milling.[20] The reaction pathways of these successful rehydrogenations are unknown. However, they appear to be sensitive to rehydrogenation conditions and particle geometry, and might be improved with a better understanding of the underlying physical and chemical processes of the hydrogenation.

We report here the first results from a closely coupled theory, characterization, and synthesis effort aimed at understanding the fundamental chemical and physical processes governing the hydrogen storage reactions of $Mg(BH_4)_2/MgB_2$. We begin with an investigation focusing on the initial hydrogenation of MgB_2, emphasizing what intermediates (if any) are formed in the hydrogenation pathway from MgB_2 to $Mg(BH_4)_2$ as the material first starts to hydrogenate. Initial hydrogenation is defined as less than 1 wt% hydrogen absorbed, out of the possible 14.9 wt% resulting from full conversion of MgB_2 to $Mg(BH_4)_2$. Sieverts measurements track the reaction itself while the other measurements characterize the reactants and products. We have applied a suite of characterization techniques that provide complementary information and distinct depth sensitivities, along with *ab initio* modeling, to probe the chemical and structural changes that accompany the initial stages of hydrogenation of MgB_2. These include methods with bulk sensitivity (200 nm–5 μm), namely Fourier transform infrared spectroscopy (FTIR), X-ray diffraction (XRD), X-ray absorption spectroscopy (XAS) in the total fluorescence yield (TFY) mode, and soft X-ray emission spectroscopy (XES). Measurements in the total electron yield (TEY) XAS mode offer the ability to separately probe surface phenomena (<5 nm for B and <48 nm for Mg) in MgB_2. These techniques and others are described in Section 2 and the ESI.† The initial hydrogenation uptake curves are introduced in Section 3.1. In Section 3.2 we discuss the results from FTIR showing the appearance of $Mg(BH_4)_2$ complexes, along with a distinct absence of features associated with potential intermediates. Section 3.3 presents the results of XAS and XES studies first showing that our MgB_2 sample is largely free of significant oxide impurities and then further elucidating the initial hydrogenation of MgB_2 with spectra complimentary to our FTIR data. These results, supported by first-principles XAS/XES simulations, demonstrate that the initial hydrogenation can involve the direct conversion of MgB_2 to $Mg(BH_4)_2$ complexes. In Section 3.4 we use density functional theory (DFT) to clarify the nature of the initially hydrogenated system. To further verify the initial hydrogenation mechanism, a kinetic model based on the reaction rate law for successive chemical processes taking place at the internal surfaces or grain boundaries is employed in Section 3.5.

2 Methods

2.1 Sample preparation and measurements

Sample handling and preparations were conducted in an Ar-filled glove-box equipped with a recirculation system that keeps H_2O and O_2 concentrations below 0.1 ppm and 0.5 ppm, respectively. Because preliminary XRD studies of commercial sources of MgB_2 indicated the presence of crystalline boron impurities, phase-pure MgB_2 was instead synthesized by room-temperature ball milling (Retsch Cryomill) the mixtures of stoichiometric amounts of Mg flakes and amorphous boron followed by heating to 650–700 °C for 16 hours in a custom-made stainless-steel cylindrical reactor under argon. The phase purity of MgB_2 was found to be very high, as evidenced by the XRD patterns shown in Fig. S1 (ESI†). XRD measurements were made using a PANalytical Empyrean diffractometer. $Mg(BH_4)_2$ was synthesized using a variation of a previously published procedure:[21] 50 mmol of 1 M $Mg(C_4H_9)_2$ in heptane (Sigma-Aldrich) was added dropwise by cannula to 190 mmol of $BH_3{\cdot}S(CH_3)_2$ (76% in dimethyl sulfide, Sigma-Aldrich) in 150 mL of dry toluene to gradually form a white precipitate of the dimethyl sulfide adduct of $Mg(BH_4)_2$. The solution was stirred under flowing Ar overnight, then the precipitate was washed several times with dry toluene and subsequently dried under vacuum at 170 °C overnight to remove the volatiles. For Sieverts measurements, the samples were transferred into the glove-box and loaded inside a sample holder with a thermocouple at the center. Pressure changes during the hydrogenation of the samples were quantified with calibrated pressure transducers and recorded using a LabVIEW-based software program. Reference measurements were also performed without any sample and with stainless steel spacers. Hydrogen capacity data are presented as weight% with respect to the MgB_2 weight. Other materials used in FTIR studies, described below, include $MgB_{12}H_{12}$ (synthesis described in the ESI†), $NaB_{10}H_{10}$ (Sigma-Aldrich), NaB_3H_8, and $BH_{0.36}$ (from colleagues, see Acknowledgements).

2.2 Spectroscopy

FTIR measurements in attenuated total internal reflectance (ATR) mode were conducted using a compact Cary 630 spectrometer located within the glovebox. The ATR crystal was diamond, and all FTIR spectra are reported as absorbance measurements.

XAS measurements were performed at beamlines (BL) 8.0.1.1 and BL 6.3.1.2 of the Advanced Light Source (ALS), Lawrence Berkeley National Laboratory (LBNL), and the resonant elastic and inelastic X-ray scattering (REIXS) BL of the Canadian Light Source (CLS). The operating pressure of the ultrahigh vacuum (UHV) endstations was $\leq 5 \times 10^{-9}$ Torr. Energy scales for Mg and B K-edge spectra were calibrated to an MgO standard and to the B–O π* resonance (193.7 eV) of a B_2O_3 powder standard, respectively. XAS data collected on BL 8.0.1.1 or REIXS were simultaneously recorded in two modes: (1) the surface-sensitive total electron yield (TEY) signal was obtained *via* measurement of the drainage current to the experimental sample, and (2) the bulk-sensitive total fluorescence yield (TFY) signal was obtained using a channeltron electron multiplier. All XAS spectra were normalized to both the incident X-ray flux, I_0, and the magnitude of the absorption edge step. I_0 was measured concurrently as the drainage current to a gold coated mesh located along the X-ray beam path and upstream of the experimental sample. The absorption edge step was taken to be the difference in the absorption intensity between the pre-edge (180 eV) and post-edge (215 eV) region for the B K-edge XAS spectra and 1290–1350 eV for the Mg K-edge measurements. The absence of X-ray beam damage was confirmed by analyzing the time dependence of the XAS TFY spectra upon rapid sequential XAS scans of $Mg(BH_4)_2$ in the same sample position, as well as upon continual movement of the sample underneath the photon beam to expose the fresh material. The relative depth sensitivities of the various methods used in this work are discussed in detail in the ESI.†

XES measurements at the B K-edge were conducted on BL 8.0.1.1 using a Rowland circle grating emission spectrometer with an area detector and at an incident photon energy of 210 eV. Energy calibration was achieved using the signals from elastically scattered photons that appear in the detector window for a series of incident X-ray energies close to the photon absorption onset. The resolution of the spectrometer was determined to be $\simeq 0.4$ eV, based upon the full width half maximum (FWHM) of the elastic peak.

2.3 *Ab initio* calculations

In order to calculate surface and intercalated hydrogen absorption energies and simulate the X-ray absorption and emission spectra (XAS/XES), first principles density functional theory calculations were performed within the Vienna Ab-Initio Simulation Package (VASP).[22–24] A plane-wave cutoff of 600 eV was used and the *k*-point sampling was chosen for each material such that the density of *k*-points is $\geq 64\,000$ per $Å^{-3}$. Pseudopotentials from the projector augmented wave (PAW) set were employed.[25] For bulk calculations, the Perdew–Burke–Ernzerhof (PBE) density functional was used.[26] The XAS/XES simulations were carried out in the VASP using an implementation that computes the required matrix elements within the PAW formalism including a self-consistent treatment of the core-hole effects on the unoccupied states.[27] Spectra were broadened with a 0.2 eV gaussian. To account for structural finite temperature effects, for each material we averaged over at least 1000 simulated spectra taken from all boron atoms within frames of *ab initio* molecular dynamics (AIMD) runs with a 0.5 fs time step at 300 K. Supercells large enough to minimize the overlap of excited core-hole states were used, typically >1000 $Å^3$.

2.4 Kinetic analysis and modeling

Kinetic analysis of the Sieverts MgB_2 hydrogen uptake data was performed by using Arrhenius fitting of the temperature dependence to extract separate barriers for each level of hydrogenation. The quality of the Arrhenius fits was also analysed as a measure of the heterogeneity of the process, since the non-Arrhenius behavior is characteristic of processes with a variety of barriers. The barriers extracted from this analysis were combined with the *ab initio* energetics calculations of molecular

H_2 dissociation and binding of atomic H to devise a kinetic model based on the fundamental reaction rate law for relevant non-equilibrium surface/interface chemical processes of the initial hydrogenation. The model couples differential equations describing H_2 dissociation and adsorption of dissociated atomic H (mediated by surface diffusion). The overall reaction may be written as $H_2(g) \leftrightarrow 2H^* \leftrightarrow 2H_{ads}$, where H* represents hydrogen at the initial dissociation site and $2H_{ads}$ represents hydrogen bound to the edges of hexagonal boron in MgB_2. The set of differential equations can be written as:

$$\frac{\partial c_{H^*}}{\partial t} = k_1 \cdot P_{H_2} - \tilde{k}_1 \cdot {c_{H^*}}^2 - \frac{\partial c_{H_{ads}}}{\partial t} \quad (1)$$

$$\frac{\partial c_{H_{ads}}}{\partial t} = k_2 \cdot {c_{H^*}}^2 \cdot {c_s}^3 \cdot (1-\theta)^2 - \tilde{k}_2 \cdot {c_s}^3 \cdot \theta^2 \quad (2)$$

Here, c_{H^*}, $c_{H_{ads}}$ are concentrations of H*, H_{ads}, respectively, in wt% H, P_{H_2} is the pressure of H_2 gas, and θ is the edge binding site (adsorption site) coverage by adsorbed hydrogen. Note that $c_{H_{ads}}$ and θ are related by $c_{H_{ads}} = f_{cv} \cdot N_s \cdot \theta$, where N_s ($=N_s^0 \cdot \exp(-E^{acc}/k_B T)$) is the number of accessible edge binding sites participating in adsorption and f_{cv} is the unit conversion factor to wt% H. We define $c_s = c_s^0 \cdot \exp(-E^{acc}/k_B T)$ as the effective concentration parameter of the accessible edge binding sites, where c_s^0 is the corresponding prefactor and E^{acc} is the associated activation energy. The kinetic coefficients k_1, $\tilde{k}_1$, k_2, and $\tilde{k}_2$ correspond to dissociation, association, adsorption, and desorption, respectively. These kinetic coefficients are expressed in the form $k_0 \cdot \exp(-E/k_B T)$, where k_0 is the prefactor, E is the activation energy, k_B is the Boltzmann constant, and T is the temperature. The activation energies E were obtained from the energy diagram in Fig. 8(b). Coverage-dependent hydrogen binding energies were estimated by computing binding energies at several coverages from DFT and fitting the result to an analytical polynomial. Kinetic prefactors k_0 were determined by multicomponent fitting to the experimental uptake data. Additional details and a table of fitted parameters can be found in the ESI.†

3 Results and discussion

3.1 Hydrogen uptake

Fig. 1 displays hydrogen uptake produced by exposure of MgB_2 to 145 bar of hydrogen at 364 °C, 378 °C, and 391 °C in a Sieverts apparatus. The uptake of hydrogen corresponds to ≃0.8–1.1 wt% H over a 120 hour exposure at all three temperatures. The uptake for full conversion of MgB_2 to $Mg(BH_4)_2$ would be 14.9 wt% H. Full hydrogenation of MgB_2 has been previously determined to require exposure to 950 bar hydrogen at 400 °C for 108 hours.[17,19] That data, and Fig. 1 reveal the kinetic limitations of MgB_2 hydrogenation. Absorption at 364 °C amounted to 0.85 wt% H, and this sample was used for subsequent studies. It should be noted that while 0.85 wt% H corresponds to only 5.7% of the full hydrogen absorption capacity, it is a significant amount of hydrogen on a molar basis. Assuming MgB_2H_x as the generic formula for the product, then 0.85 wt% H corresponds stoichiometrically to $MgB_2H_{0.39}$; per formula unit of MgB_2, 39 mol% of the sample could potentially be affected by this level of hydrogenation. The results of dehydrogenation measurements from the initially hydrogenated MgB_2 sample are plotted in Fig. S11 of the ESI.†

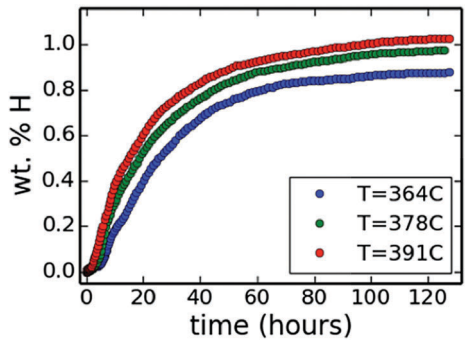

Fig. 1 Hydrogen uptake for MgB_2 exposed to hydrogen gas at 145 bar pressure in a Sieverts apparatus for three different temperatures: 364 (lower curve), 378 (middle), and 391 (upper) °C.

3.2 FTIR

The samples were examined with FTIR in order to more clearly identify reaction products and possible intermediates. Fig. 2(a) shows an FTIR spectrum of MgB_2 and MgB_2 containing 0.85 wt% H. For reference, an FTIR spectrum of $Mg(BH_4)_2$ is shown, taken with the same AT-FTIR instrument and under identical experimental conditions to those for the MgB_2 and MgB_2 + 0.85 wt% H samples.

Fig. 2(a) shows that FTIR spectral features attributed to the B–H bending modes of $Mg(BH_4)_2$ arise upon initial hydrogenation of MgB_2. Also presented in Fig. 2(a) is a composite spectrum obtained by multiplying the experimental $Mg(BH_4)_2$ spectrum by 4.9% and adding it to the spectrum of as received MgB_2. This composite spectrum is meant to mimic a sample in which 4.9% of the B atoms have been hydrogenated to $Mg(BH_4)_2$ (corresponding to 0.85 wt% H converted completely to $Mg(BH_4)_2$), with the remaining 95.1% of the sample being MgB_2. The correlation in intensities and peak positions is striking, particularly for the characteristic doublet of peaks in the pure $Mg(BH_4)_2$. A small shift is observed in the peaks from the initially hydrogenated sample with respect to the composite spectrum, which may be attributable to the increased slope of the spectrum acquired from the hydrogenated sample. The spectra displayed in Fig. S3 (ESI†) show that this shift in the wavenumber is much smaller than the range of shifts reported in the literature for B–H bending frequencies for a variety of different borohydrides. As such, we assert that the close similarity of the composite FTIR spectrum to that of MgB_2 + 0.85 wt% H in Fig. 2(a) is due to the formation of $Mg(BH_4)_2$ during the early stages of hydrogenation.

These results imply that B–H reaction intermediates of the type observed during dehydrogenation are not being formed as persistent by-products during initial hydrogenation. We directly assessed this implication by looking for intermediates in the FTIR of the MgB_2 + 0.85 wt% H sample. Fig. 2(b) shows FTIR data recorded under identical experimental conditions for

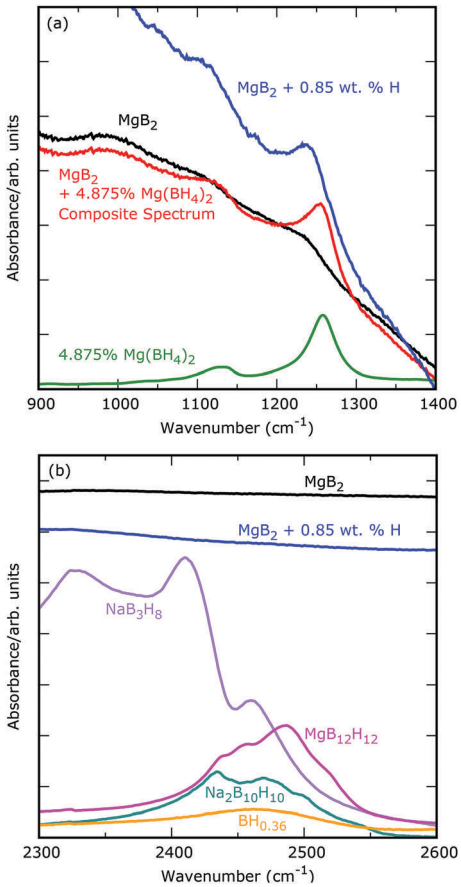

Fig. 2 (a) FTIR data for as received MgB_2 compared to MgB_2 hydrogenated to 0.85 wt% H. Also shown is an FTIR spectrum of a sample of $Mg(BH_4)_2$ (multiplied by 0.049) and a composite spectrum made by adding the scaled $Mg(BH_4)_2$ FTIR spectrum to the spectrum of MgB_2. (b) FTIR data at higher wavenumbers for MgB_2 and MgB_2 hydrogenated to 0.85 wt% H. Also depicted are FTIR spectra for $BH_{0.36}$, $Na_2B_{10}H_{10}$, NaB_3H_8 and $MgB_{12}H_{12}$ monohydrate.

MgB_2, initially hydrogenated MgB_2 (MgB_2 + 0.85 wt% H), and a number of experimental standards analogous to intermediates that could potentially form during the initial stages of hydrogenation, specifically $MgB_{12}H_{12}$, NaB_3H_8, $Na_2B_{10}H_{10}$, and $BH_{0.36}$. (The $BH_{0.36}$ sample is a nanoparticulate material with terminal B–H bonds surrounding a B cage structure.) All of these compounds produce a terminal B–H stretch in the spectral region shown in Fig. 2(b) (2300–2600 cm^{-1}), a region that is featureless in the MgB_2 and initially hydrogenated MgB_2 samples. Since the FTIR data have a high statistical quality, we estimate (see Fig. S5 and S6, ESI†) that B–H stretches would be observed in the initially hydrogenated MgB_2 if the reaction intermediates were present at molar concentrations as little as $\simeq$0.5%. No such peaks are observed in the FTIR data for the initially hydrogenated MgB_2, which, to within 0.5% sensitivity, indicates that there is no $[B_3H_8]^-$, $[B_{10}H_{10}]^{2-}$, $[B_{12}H_{12}]^{2-}$, or delocalized B–H being produced. The only product of hydrogenation in any significant quantity is $Mg(BH_4)_2$. The absence of a structure in the FTIR spectrum of Fig. 2(b) from the initially hydrogenated MgB_2 also allows us to exclude the formation of a trapped B_2H_6 intermediate, which would give B–H terminal stretches in the window of Fig. 2(b).

3.3 XES and XAS

XAS from MgB_2 (with varying levels of oxide contamination) at the B K-edge has been extensively investigated[28–31] in the early 2000s as a probe of the electronic structure to aid in understanding the superconductivity of MgB_2. It is well established that the incompletely filled bonding σ bands are mostly $2p_{xy}$ in character and are thought to play an important role in the superconductivity of MgB_2.[32,33]

Fig. 3(a) compares B K-edge XAS measured in both TEY and TFY modes for two samples of MgB_2. It is evident from comparison with the B_2O_3 reference that one of the MgB_2 samples is significantly less oxidized than the other. This is due to the implementation of improved sample handling procedures. The surface sensitivities of the TEY and TFY modes of detection are $\simeq$5 nm (TEY) and 175 nm (TFY), respectively, at the B K-edge. The TFY spectrum of the oxidized sample shows a sharp initial peak at 186.8 eV, which corresponds to electron transitions from the B 1s state to unoccupied $2p_{xy}$ states just above the Fermi level. Significantly, this feature is absent in the TEY data of the more oxidized MgB_2 sample, which instead displays only features associated with the presence of boron oxide.

The origin of this difference between the TEY and TFY signals is attributed to surface oxidation, which arises upon exposure of the sample to the glove box environment over the course of several months, or during sample handling in environments with sub-optimal water and oxygen partial pressures. Since the B K-edge TEY data have $\simeq$35 times higher surface sensitivity than the TFY measurements, the TEY spectra are affected more by the presence of boron oxide formed during oxidation of the MgB_2 surface. Significantly, samples that were aged *via* exposure to glove box conditions in excess of 6 months exhibited a TFY spectrum consistent with the presence of only boron oxide, indicating that surface oxidation would continue to a depth of at least 175 nm. To minimize the degree of surface oxidation, a revised sample preparation protocol was implemented prior to repeating the B K-edge XAS measurements of MgB_2 on the "pristine" sample: freshly synthesized (<1 week) MgB_2 was used, and the sample was stored in a glove box with <0.1 ppm of H_2O and <0.5 ppm of O_2. The samples were then transported under Ar in hermetically sealed double envelopes, loaded into the spectrometer vacuum system in an ultra-high-purity argon environment in a glove bag with a humidity meter that can detect $\geq$25 ppm water, and then transferred to the load lock of the XAS endstation within 15 minutes. The pressure in the load lock was then reduced to $<10^{-7}$ Torr in under $\simeq$30 minutes. The resulting B K-edge XAS spectra for TEY and TFY collection modes are shown at the bottom of Fig. 3(a) for the "pristine" MgB_2 sample.

As observed in Fig. 3(a), both the B K-edge TEY and TFY XAS MgB_2 "pristine" sample spectra show the leading-edge feature corresponding to $2p_{xy}$ final states. This agreement indicates that the sample is largely free of oxidation, although we cannot exclude it at the level of several Å. Thus, meaningful XAS spectra for the $Mg(BH_4)_2/MgB_2$ system can be produced and interpreted.

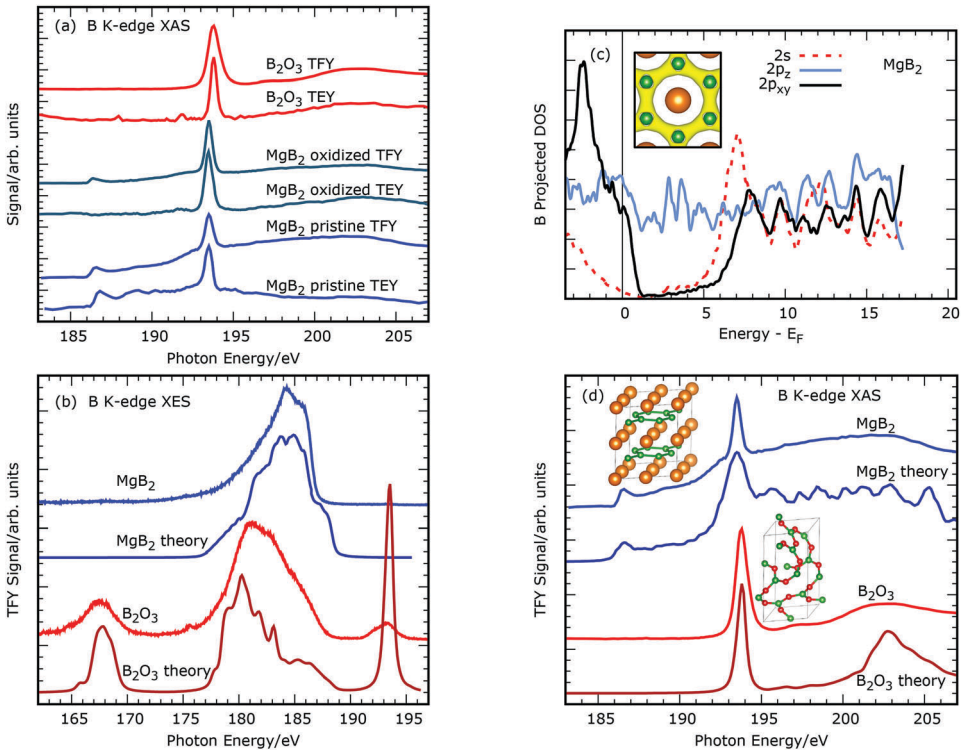

Fig. 3 (a) Experimental B K-edge TEY and TFY XAS data for two MgB_2 samples and a sample of B_2O_3, showing the effects of oxidation on the TEY spectrum, as described in the text. (b) Experimental and simulated B K-edge XES for MgB_2 and B_2O_3. (c) The orbital-angular-momentum-resolved density of states (DOS) for MgB_2, aligned with XAS data directly below; inset: the calculated $2p_{xy}$ charge density isosurface (yellow) of the sp^2 binding of the atoms in the boron plane (green spheres). (d) Experimental and simulated B K-edge TFY XAS for MgB_2 and B_2O_3; insets: MgB_2 and B_2O_3 structures with Mg, B, and O atoms shown in orange, green, and red, respectively.

Fig. 3(d) compares the experimental B K-edge TFY XAS spectrum of MgB_2 to our theoretical prediction for this spectrum. We also show in Fig. 3(d) a B K-edge XAS TFY spectrum of the B_2O_3 standard sample along with the theoretical prediction for B_2O_3. The orbital angular momentum contributions to the simulated MgB_2 XAS spectra are presented in Fig. 3(c) in the form of the orbital projected electronic density of states (DOS).

The leading edge MgB_2 XAS feature at 186.8 eV incident photon energy is predicted to correspond to B $2p_{xy}$ states just above the Fermi level, in agreement with prior assignments.[28–31] This assignment is consistent with the calculated MgB_2 spectrum and the projected DOS in Fig. 3(c) and (d). The charge density isosurface of the sp^2 hybridized in-plane boron states, corresponding to this p_{xy} feature, is presented in the Fig. 3(c) inset. One can see from the $2p_{xy}$ isosurface that this charge is associated with the physical integrity of the B hexagonal structure. Thus, reaction pathways that disrupt this B plane are readily monitored by the $2p_{xy}$ feature in the XAS.

The calculated B_2O_3 XAS features match well to the reference B_2O_3 spectrum, specifically the strong peak at 193.7 eV and the broader feature near 203 eV. These features can be seen to originate from boron 1s absorption into the boron 2p orbitals predicted to be near 6.5 eV and 16.0 eV above the Fermi level, shown in the calculated DOS in Fig. S7 (ESI†). The simulated spectra indicate that both B_2O_3 and MgB_2 should exhibit a resonance at photon energies near 193.7 eV, originating from planar three fold coordinated boron atoms in both structures, *i.e.*, boron is surrounded by three other boron atoms in MgB_2 and by three oxygen atoms in B_2O_3, as shown in the Fig. 3(d) insets. The presence of a peak close to 193.7 eV for MgB_2 is consistent with the experimental XAS data reported by Kurmaev *et al.* for a sample measured immediately after it was cleaved under UHV conditions (*i.e.*, with presumed minimal surface oxide).[31] Therefore, it is proposed that the resonance at $\simeq$193.7 eV in the experimental XAS presented in Fig. 3(a) and (d) contains contributions from both B_2O_3 and MgB_2, with the MgB_2 component causing the observed peak asymmetry.

Fig. 3(b) displays the B K-edge XES data for "pristine" MgB_2 and the B_2O_3 reference. The features observed at 167.6 eV and 193.2 eV in the XES data for B_2O_3 are distinct and well-separated from the MgB_2 XES spectral envelope, allowing a clear assessment of the extent of sample oxidation. MgB_2 XES has only trace oxide signals at 167.6 eV and 193.2 eV. The height of these features compared to the B_2O_3 XES data indicates very low levels of oxidation, $\simeq$3.8 mol%, which offers further evidence that the XES and XAS spectra can be interpreted without ambiguity. The theoretical predictions for these MgB_2 and B_2O_3 XES spectra are shown in Fig. 3(b). The theory indicates that the B_2O_3 XES features at 168 eV and 194 eV are due to B 2p states deep in the valence band and at the minimum of the conduction band, respectively.[34,35]

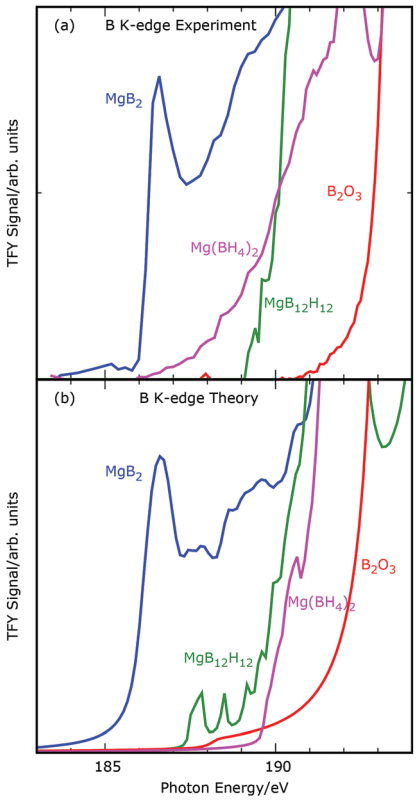

Fig. 4 (a) Experimental B K-edge TFY XAS data for MgB_2 compared to $MgB_{12}H_{12}$, $Mg(BH_4)_2$, and B_2O_3. (b) Theoretical B K-edge TFY XAS spectra for MgB_2 compared to $MgB_{12}H_{12}$, $Mg(BH_4)_2$, and B_2O_3.

Fig. 4(a) displays a comparison of the near edge region of the TFY B(1s) XAS spectra of MgB_2, B_2O_3, and boron species in partially hydrogenated ($MgB_{12}H_{12}$, H : B ratio 1 : 1) and fully hydrogenated ($Mg(BH_4)_2$, H : B ratio 4 : 1) states. It is evident from the inspection of these data that the unoccupied $2p_{xy}$ state of MgB_2 induces the only resonance observed between $\simeq$185 and 187.5 eV. As such, the $2p_{xy}$ resonance provides an excellent diagnosis of the presence and, in principle, the amount of MgB_2 within the depth probed by the XAS-TFY measurements.

The loss of the resonance at $\simeq$186.8 eV upon conversion of MgB_2 to other boron based materials can be accounted for theoretically *via* calculation of the predicted XAS spectra in tandem with the electronic density of states, including the specific treatment of the $2p_{xy}$ state for MgB_2, $MgB_{12}H_{12}$, $Mg(BH_4)_2$, and B_2O_3. The simulated spectra, Fig. 4(b), are consistent with the measured spectra. As can be seen in the density of states for MgB_2 in Fig. 3(c), and for $MgB_{12}H_{12}$, $Mg(BH_4)_2$, and B_2O_3 in Fig. S7 (ESI†), only MgB_2 has an appreciable number of unoccupied states at the top of the valence band. Relative to the Fermi level, the valence band maximum is lower for $MgB_{12}H_{12}$, $Mg(BH_4)_2$, and B_2O_3. Therefore, the top of the B $2p_{xy}$ band is occupied for these materials and cannot contribute to the core-level X-ray absorption. Furthermore, we note that the conduction bands for $MgB_{12}H_{12}$, B_2O_3, and $Mg(BH_4)_2$ are at high enough energies that no resonances can appear in the 186.8 eV region corresponding to the $2p_{xy}$ states of MgB_2.

Based on the evolution of the 186.8 eV XAS resonance as a signature of conversion of MgB_2, we now consider the effects of the initial hydrogenation of MgB_2 on the XAS, specifically for the absorption of 0.85 wt% of H (0.39 mol% H) under the following transformation: $MgB_2 + (0.39/2)H_2$ (360 °C, 140 bar) → $MgB_2H_{0.39}$. Possible effects on the intensity of the $2p_{xy}$ feature depend on the possible intermediates being formed, and are as follows:

(1) $MgB_2 + (0.39/2)H_2 \rightarrow (0.951)MgB_2 + (0.049)Mg(BH_4)_2$: 4.9% of the B atoms transform into $Mg(BH_4)_2$. Since the $2p_{xy}$ feature disappears for $Mg(BH_4)_2$, we would expect a 4.9% reduction in the intensity of the $2p_{xy}$ feature in TFY XAS.

(2) $MgB_2 + (0.39/2)H_2 \rightarrow (0.805)MgB_2 + (0.1625)Mg + (0.0325)MgB_{12}H_{12}$: 19.5% of the B atoms in the sample transform into $MgB_{12}H_{12}$. Since the $2p_{xy}$ feature disappears for $MgB_{12}H_{12}$, we would expect a 19.5% reduction in the intensity of the $2p_{xy}$ feature in TFY XAS.

(3) $MgB_2 + (0.39/2)H_2 \rightarrow (0.805)MgB_2 + (0.39)B + (0.195)MgH_2$: 19.5% of the Mg atoms transform into MgH_2. In this case, one should observe significant accumulation of elemental boron (from 19.5% of the B atoms) and concomitant reduction of features associated exclusively with MgB_2. To more directly probe this possibility, we also consider this case using Mg K-edge XAS, as described below.

To explore these three potential effects of initial hydrogenation, B K-edge XAS TFY was recorded for MgB_2 + 0.85 wt% hydrogen and a comparison with the XAS data from MgB_2 is displayed in Fig. 5. Direct comparison of the resonance intensities is appropriate for the data presented in Fig. 5, as they were recorded under identical experimental conditions (during the same experimental run) and the data were normalized to the incident flux and the magnitude of the absorption edge step (which yields a 'per boron atom' spectrum). Remarkably, the $2p_{xy}$ resonance is largely unaffected by the addition of H; in fact, the change in the resonance intensity is on the order of the error in the measurement. This behavior is inconsistent with the 19.5% drop in intensity expected for conversion of MgB_2 to $MgB_{12}H_{12}$, which should be readily observed. By the logic set forth in 1–3 above, the insensitivity of the $2p_{xy}$ feature to initial hydrogenation eliminates the possibility of $MgB_{12}H_{12}$ or MgH_2 formation in any significant quantity. The only remaining possibility is highly selective hydrogenation of MgB_2 to yield $Mg(BH_4)_2$ complexes.

Fig. 5(b) displays predicted XAS spectra for two composite materials, represented by linear combinations of the pure material simulated spectra. These correspond to the limiting cases for uptake of 0.85 wt% H by MgB_2: (1) 95.1% MgB_2:4.9% $Mg(BH_4)_2$ and (2) 80% MgB_2:20% $MgB_{12}H_{12}$, where the percentages refer to the proportion of B atoms belonging to each material in the composite. The calculated spectra for pure MgB_2 and $Mg(BH_4)_2$ are also depicted for the purposes of direct comparison. It is evident from inspection that these simulations support the conclusions drawn above from the experimental spectra. If the absorbed hydrogen is contained solely in $MgB_{12}H_{12}$, the drop in the $2p_{xy}$ feature would be evident experimentally, while the change in intensity would be on the

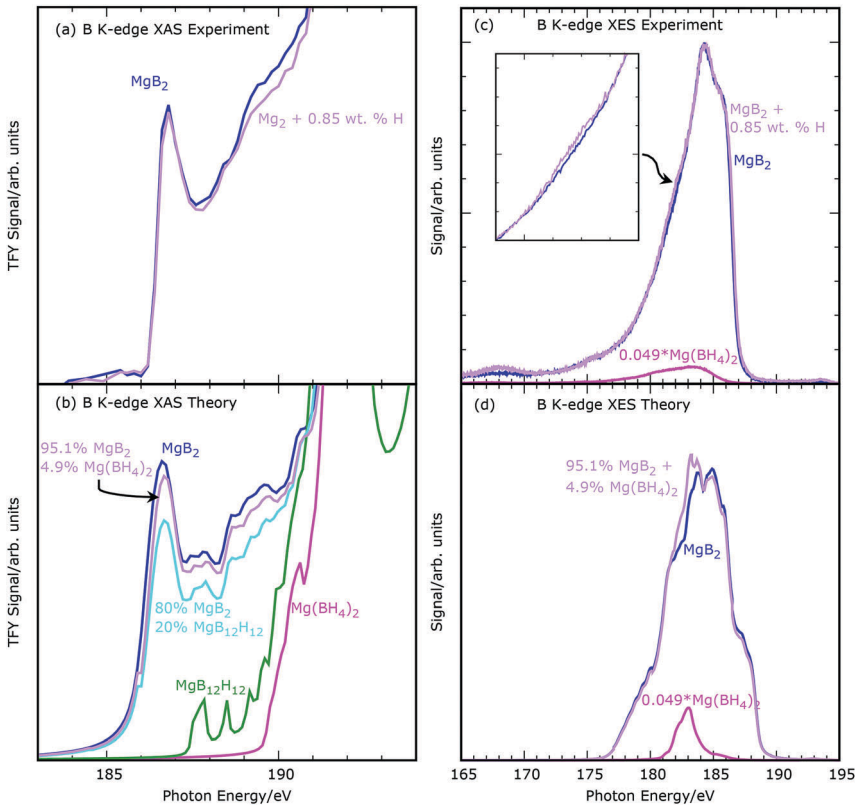

Fig. 5 (a) Experimental B K-edge TFY XAS data for MgB_2 compared to MgB_2 + 0.85 wt% H. (b) Theoretical prediction for the change in the XAS $2p_{xy}$ spectral peak with varying types of hydrogenation at the 0.85 wt% H level. (c) B K-edge XES data for MgB_2 compared to MgB_2 hydrogenated to 0.85 wt% H. (d) Theoretical B K-edge XES spectra for MgB_2 compared to MgB_2 hydrogenated to 0.85 wt% H in the form of $Mg(BH_4)_2$.

order of experimental error if hydrogen is absorbed by $Mg(BH_4)_2$ and may not be clearly observed.

Fig. 5(c) compares experimental B K-edge XES data for MgB_2 to MgB_2 hydrogenated to 0.85 wt% H. As with the TFY XAS spectra of Fig. 3, the two spectra are very similar, supporting the notion that a minimal number of B atoms have been affected by the hydrogenation. This is consistent with the conclusion from XAS that $Mg(BH_4)_2$ is being formed directly, with no evidence for the large (19.5%) B spectral changes that would be produced by the formation of compounds with smaller H : B ratios, namely $MgB_{12}H_{12}$, $Mg(B_{10}H_{10})$, or $Mg(B_3H_8)_2$.

Fig. 5(d) shows the theoretical predictions for the XES spectra of MgB_2 and MgB_2 + 4.9 mol% H in the form of $Mg(BH_4)_2$ complexes. With this result it is evident that the intensity increase near 182 eV in the experimental initially hydrogenated spectrum in comparison to the as-received MgB_2 spectrum (see the inset Fig. 5(c)) can be associated with the formation of $Mg(BH_4)_2$.

XAS measurements were also performed at the Mg K-edge to further investigate the chemical changes induced during the initial stages of hydrogenation, and to provide an additional probe that can be specifically sensitive to the presence of MgH_2. Fig. 6 displays XAS data for MgB_2, initially hydrogenated (0.85 wt% H) MgB_2, and standards corresponding to several possible intermediates ($Mg(BH_4)_2$, MgH_2 and $MgB_{12}H_{12}$) that could potentially form during hydrogenation.

The spectral features observed in Fig. 6 are much broader than those in the B K-edge XAS data because of the increased lifetime broadening of the Mg K core-hole state. Nonetheless, spectral variations are readily observed, indicating that, when B is hydrogenated, changes are also observed in the electronic structure of the associated Mg. The depth sensitivity of the Mg K-edge TFY XAS data is $\simeq$12 000 nm. It is observed that there is a small decrease in the intensity of the leading edge at 1299.5 eV associated with initial hydrogenation. Also, there are small relative changes in intensity over the energy range 1303–1313 eV. None of the standard samples of MgH_2, $Mg(BH_4)_2$ and $MgB_{12}H_{12}$ exhibit any leading-edge intensity at 1299.5 eV and therefore their formation could produce the decrease in the XAS intensity seen at this position upon hydrogenation. However, the spectral changes over the energy range 1303–1313 eV are most consistent with the formation of $Mg(BH_4)_2$. In particular, XAS of MgH_2, which has a rather flat spectral profile over the range 1303–1313 eV cannot account for the selective increase in intensity at 1308.6 eV seen in the MgB_2 + 0.85 wt% H sample and strongly suggests that MgH_2 is not present in significant quantities. If MgH_2 was being exclusively formed, then 19% of the Mg K-edge XAS signal from MgB_2 would have been modified towards that of MgH_2, which is clearly not seen. The XAS signals for $Mg(BH_4)_2$ and $MgB_{12}H_{12}$ are very similar over the energy range 1303–1313 eV, but the strong shoulder seen in the $MgB_{12}H_{12}$ spectrum at 1315 eV is not seen in the

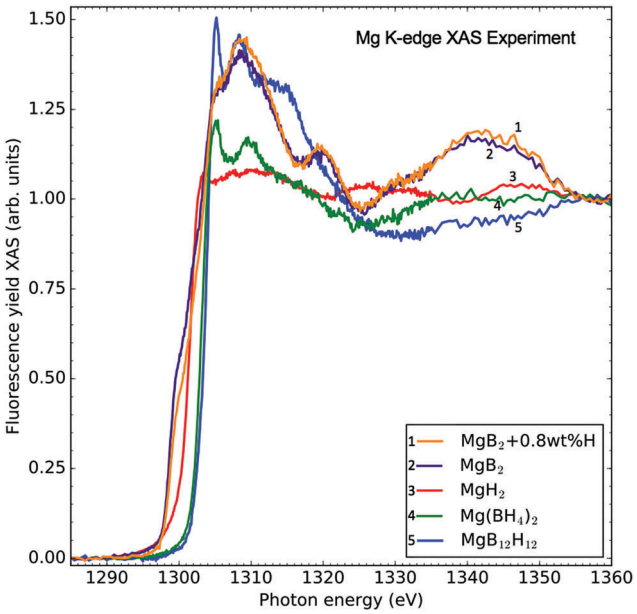

Fig. 6 Mg K-edge TFY XAS data for MgB_2, MgB_2 + 0.85 wt% H, and samples of $Mg(BH_4)_2$, MgH_2, and $MgB_{12}H_{12}$.

initially hydrogenated MgB_2 sample. Based on this, we conclude that the Mg K-edge spectral variations are most consistent with the formation of $Mg(BH_4)_2$, which would support the assignment made from the FTIR and B K-edge XAS data. XRD analysis of the partially hydrogenated MgB_2 samples showed no crystalline phases other than MgB_2, suggesting that the small amount of $Mg(BH_4)_2$, representing 4.9% of the boron atoms, may be amorphous.

3.4 Possible binding sites for atomic H

To support our experimental FTIR, Sieverts hydrogen uptake, and XAS/XES results and calculated XAS/XES and DOS showing that the initial hydrogenation of MgB_2 contains highly hydrogen coordinated boron (*i.e.* $Mg(BH_4)_2$), we have theoretically investigated several possible initial absorption mechanisms. First of all, MgB_2, being a layered material, might be suspected to intercalate hydrogen before the more drastic structural and chemical rearrangements into $Mg(BH_4)_2$. To explore this possibility we consider the intercalated structure in the formalism of density functional theory.

The intercalated structure involves placing H atoms with a population consistent with 0.85 wt% H (39 mol% relative to the MgB_2 formula unit) uniformly between the B hexagonal sheet and the Mg layer, with bridge binding across two adjacent B atoms. The calculated formation energy of this intercalated structure is +0.74 eV per H atom, showing that this form of absorption is thermodynamically highly unfavorable. Thus, this scenario may be ruled out. Our calculations show that if H is intercalated, then clustering of H together on a single B atom (required to form $Mg(BH_4)_2$) would be even more energetically unfavorable (up to 0.17 eV per H) than the uniform intercalated distribution (which is itself unfavorable). We note that calculations by Wang *et al.* showed that the diffusion of H intercalated into MgB_2 should be rapid if its formation could be made thermodynamically favorable.[36]

As additional confirmation that H intercalation can be excluded, we have calculated the B K-edge XAS spectrum for the intercalated structure, with the results shown in Fig. S7 (ESI†). We found that even with only 0.85 wt% of added hydrogen, if the H intercalates, the B $2p_{xy}$ XAS spectral feature at 186.8 eV completely disappears for all boron, not just those bonded to hydrogen, contradicting the experimental results depicted in Fig. 5(a). Thus, for energetic reasons, and incompatibility with the experimental XAS findings, we can rule out H intercalation as the geometry for the initial hydrogenation of MgB_2. Interestingly, hydrogen absorption is possible between layers of $SrGa_2$ and $SrAl_2$, producing $SrGa_2H_2$ and $SrAl_2H_2$.[37,38] $SrGa_2$ and $SrAl_2$ form structures similar to MgB_2, however, the hexagonal Ga net of $SrGa_2$ is puckered. In these materials, the hydrogen atoms bind directly above or below Ga/Al atoms, and once hydrogenated, both materials exhibit puckered hexagonal sheets.

As a second possibility, we have investigated the mechanism associated with the adsorption of H on the boron edge sites of the $(10\bar{1}0)$ MgB_2 surface, as shown in Fig. 7(a). This surface is

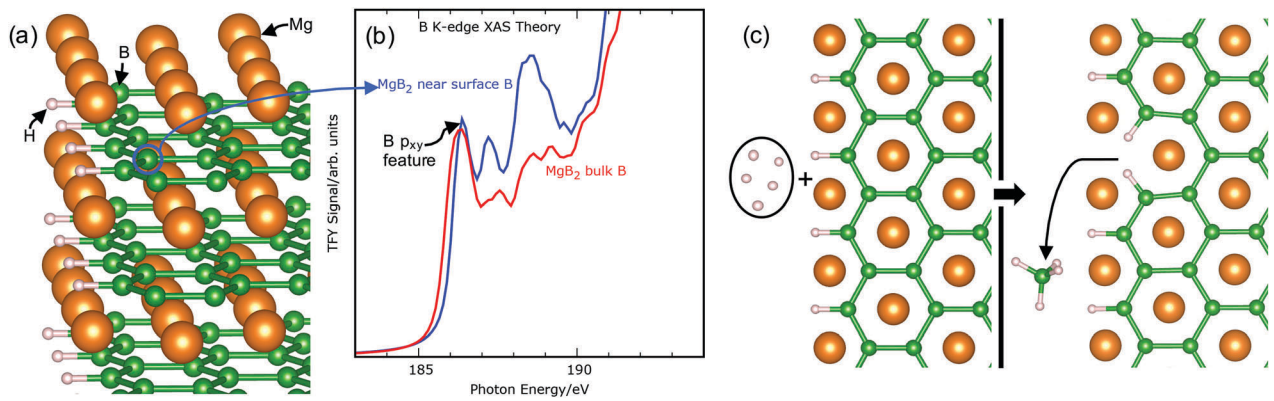

Fig. 7 (a) Hydrogen monolayer absorbed on the $(10\bar{1}0)$ surface on the left of the image. H, B, and Mg atoms are given by tan, green, and orange spheres, respectively. (b) B K-edge simulated XAS of the p_{xy} feature of a MgB_2 bulk B atom and a B atom near the $(10\bar{1}0)$ surface. The near surface B atom is indicated with a circle in (a). (c) Depiction of the $(10\bar{1}0)$ surface process of binding of five additional hydrogen atoms by the creation of a $[BH_4]^-$ anion, a surface defect, and 1 additional surface adsorbed hydrogen atom, viewed from the [0001] direction.

the second lowest energy low index surface[39] and unlike the lowest energy surface, the Mg-terminated (0001) basal plane, it contains open boron sites. Due to the low surface energy and the condition that MgB_2 crystallites cannot be terminated by basal planes alone, it is probable that the $(10\bar{1}0)$ surface exists at the edges or grain boundaries of the powdered MgB_2 samples used in the hydrogenation experiments reported in this work. We calculate that the adsorption energy of an isolated H in the dilute limit on this surface is −0.93 eV, and that the average adsorption energy for a monolayer, depicted in Fig. 7(a), is −0.59 eV per H. The zero of energy for these calculations is the energy of an isolated H_2 molecule in the gas phase and the bare $(10\bar{1}0)$ MgB_2 surface at zero temperature. As such, the adsorption of H on the $(10\bar{1}0)$ surface should be thermodynamically favorable, even under reaction conditions. Furthermore, as shown in Fig. 7(b), the MgB_2 B $2p_{xy}$ XAS feature is retained for boron atoms that are neighbors to the hydrogen-bound edge borons. Therefore, the $(10\bar{1}0)$ surface hydrogen adsorption does not appreciably influence the electronic structure of the bulk MgB_2 boron atoms, which is consistent with the experimental spectra, Fig. 5(a), in which the p_{xy} feature is retained in the initially hydrogenated MgB_2 sample.

However, binding of single H atoms to B edge sites is unlikely to account for the full magnitude of absorption observed experimentally because the H to B ratio of surface adsorption in this scenario would be too low, requiring $\simeq$20% of the boron atoms to be surface atoms or defects. Instead, clustering of H to the available boron edges to produce $[BH_4]^-$ units is more likely, consistent with the experimental results. This reaction can continuously take place by consuming (or etching) the boron from these edge binding sites inward. The enthalpy of binding five additional H atoms on the $(10\bar{1}0)$ MgB_2 surface (in addition to an adsorbed H monolayer, see Fig. 7(a) and (c), left hand sides), producing a $[BH_4]^-$ unit bound to the surface, a surface B vacancy, and the adsorption of one additional hydrogen on the surface is calculated to be −0.91 eV (−0.18 eV per H atom adsorbed). This value is established relative to the surface in Fig. 7(a) and H atoms in the form of H_2. The process is depicted on the right side of Fig. 7(c).

3.5 Mechanistic process of hydrogen incorporation

Our combined experiment-theory analysis strongly suggests that in the initial stages of uptake, hydrogen tends to accumulate and form σ-bonds to boron. Probable sites include exposed reactive MgB_2 edges (*i.e.*, $(10\bar{1}0)$ surfaces) as explored in our models, as well as high-energy strained B–B bonds associated with grain/domain boundaries or lattice point defects. Initial hydrogenation therefore occurs as a solid-state interfacial reaction rather than *via* diffusion of atomic hydrogen into bulk MgB_2. This process could proceed *via* direct dissociative adsorption of molecular H_2 on the eventual binding sites, or else *via* initial H_2 dissociation elsewhere followed by diffusion of atomic hydrogen to these sites. Because spectroscopic evidence is insufficient to distinguish between these possibilities, we next invoke kinetic modeling to explore and validate mechanistic details of hydrogen incorporation.

An initial clue into the mechanism can be discerned by extracting the effective activation energy as a function of hydrogenation from the temperature-dependent rates in Fig. 1 assuming the Arrhenius law. Fig. 8(a) shows the analyzed activation energy barrier profile, along with the quality of the Arrhenius fits. Significantly, the analysis shows that there are at least two distinct kinetic regimes. The very initial uptake region (<0.25 wt% H) exhibits a higher barrier and a poorer Arrhenius fit, indicating a heterogeneous process that is less well described by a unique, well-defined barrier. At the same time, this regime actually displays a faster overall rate despite having a higher barrier, which implies an unusually high prefactor. The likely interpretation of the heterogeneity and high prefactor is that the behavior conveys a surface process with a large number of accessible sites rather than a bulk process. The most obvious explanation is molecular H_2 dissociation on exposed surfaces. In fact, the magnitude of the associated barrier in Fig. 8(b) ($\simeq$0.91 eV) is quite similar to the H_2 dissociation barrier on Mg-terminated MgB_2 basal planes computed by Wang *et al.* ($\simeq$0.89 eV).[39] These basal planes are the most stable among MgB_2 surfaces, implying that they should be relatively commonly exposed. This translates to a high density of available surface dissociation sites, which would explain the high observed rate.

On the other hand, the range from 0.2 to 0.7 wt% H in Fig. 8(a) exhibits a much lower barrier and a flatter energy barrier profile with more regular Arrhenius characteristics (*i.e.* with a higher R^2 correlation value). We speculate that this regime is associated with diffusion and binding of atomic hydrogen to boron sites at the reactive interface. We refer to this second regime as a collective ''diffusive adsorption'' process, which reflects the thermodynamic driving force for atomic hydrogen to migrate and bind to boron following initial H_2 dissociation (*e.g.*, on Mg-terminated basal plane sites). The rate analysis confirms that different rate-limiting processes dominate depending on the level of hydrogenation. It also shows that in the initial uptake mechanism, H_2 dissociation and H binding can be categorized as distinct stages, supporting the interpretation that the two processes likely occur at different reaction sites. Note that this explanation is compatible with the energetic preference of hydrogen to segregate to high-energy boron sites, which should also be fewer in number than the basal-plane molecular dissociation sites.

The barriers obtained from Fig. 8(a) were combined with the *ab initio* energetics calculations described in the previous section to construct a full energy landscape for the initial hydrogenation process. This landscape, shown in Fig. 8(b), describes H_2 dissociation followed by diffusive adsorption of atomic hydrogen to form σ-bonds to boron within MgB_2. Here, we have assumed that dissociation occurs on Mg-terminated basal planes, in agreement with the calculations of Wang *et al.*,[39] while the eventual destination for hydrogen following diffusive adsorption is the collection of boron edge sites.

The energy landscape in Fig. 8(b) was used to parameterize kinetic equations describing the dissociation and diffusive adsorption processes based on local concentrations of the

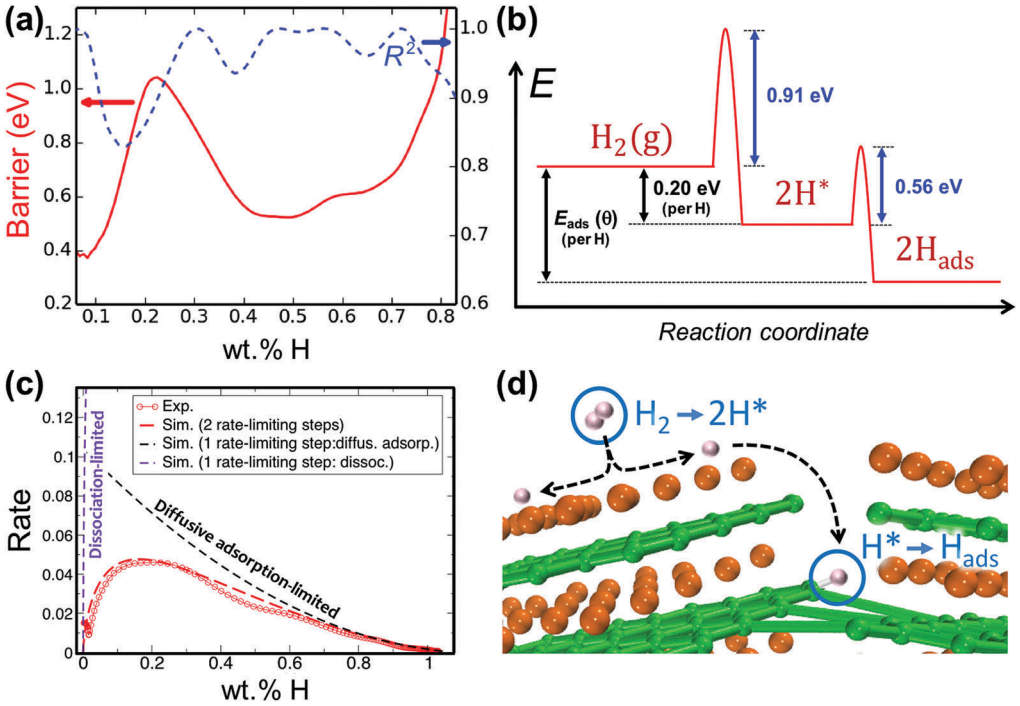

Fig. 8 (a) Calculated activation barrier for initial hydrogenation of MgB_2 (eV per formula unit) based on Arrhenius analysis of the data in Fig. 1. The R^2 correlation coefficient for the linear fits to the Arrhenius equation are also shown. (b) Energy profile for initial hydrogenation based on a two-step mechanism corresponding to dissociation ($H_2 \rightarrow 2H^*$) and diffusive adsorption ($H^* \rightarrow H_{ads}$). Binding and coverage-dependent adsorption energies are from *ab initio* calculations, whereas barriers are derived from the Arrhenius analysis. (c) Comparison between simulated and measured hydrogen uptake curves for MgB_2 at 145 bar H_2 at 391 °C. (d) Schematic of the proposed reaction mechanism, whereby H_2 dissociates on exposed basal-plane surfaces with Mg termination and then migrates as atomic hydrogen to attack high-energy B–B bonds. Subsequent collection of hydrogen at the boron edges results in the formation of $Mg(BH_4)_2$ complexes.

intermediate H* (upon dissociation) and product H_{ads} (following σ-bond formation between hydrogen and boron). The governing differential equations for these processes, which also consider the competing backward reactions of association and desorption, are listed in Methods. More complete descriptions can also be found in the ESI.† Note that hydrogen binding energies carry a dependence on coverage, which was estimated by fitting to DFT calculations as described in Methods and in the ESI.†

Simulations of hydrogen uptake behaviors were carried out by numerically solving the coupled kinetic equations for the same three temperatures employed for the experiments (T = 364, 378, and 391 °C), with kinetic prefactors used as fitting parameters. Fig. S10 (ESI†) shows the comparisons of the isotherm uptake simulations, from which it is clear that the major features and trends of the experimental results for different temperatures are generally well reproduced by our kinetic models (the results for 391 °C are shown in Fig. 8(c)). The agreement suggests that our interpretation of the two processes in Fig. 8(a) and (b) as dissociation and diffusive adsorption is valid.

Next, we conducted controlled simulations by manipulating the relative rates of the two operating reactions for initial hydrogenation (dissociation and diffusive adsorption). Specifically, the rate for each reaction was artificially increased to remove all associated kinetic limitations, allowing us to explore the possibility of a single rate-determining reaction in lieu of the proposed two-step process. Simulated rate curves for reactions limited entirely by dissociation (purple dashed line) and entirely by diffusive adsorption (black dashed line) are shown in Fig. 8(c). Notably, neither of these limits is able to qualitatively describe the experimentally observed behavior across the range of initial hydrogenation, confirming a two-step reaction process. Instead, rates at the early reaction stages are consistent with dissociation limitations, whereas the later stages are consistent with diffusive adsorption limitations that reduce the hydrogenation rate as the available adsorption sites become saturated. The resulting initial hydrogenation mechanism that agrees with the Arrhenius analysis of the experimental data, the kinetic models, and the spectroscopic evidence is shown schematically in Fig. 8(d): (1) H_2 dissociation, probably on Mg-terminated MgB_2 basal planes, followed by (2) diffusive adsorption and the formation of B–H bonds as atomic hydrogen migrates to high-energy boron sites, and (3) hydrogen buildup at these sites to form $Mg(BH_4)_2$ complexes.

It is worth noting that beyond 0.7 wt% H, the Arrhenius analysis in Fig. 8(a) suggests the onset of a possible new kinetic regime with a higher barrier. This likely represents the beginning of a deeper hydrogenation state, possibly associated with the nucleation of a condensed phase. This higher barrier is probably responsible for the saturation of the hydrogen content under the Sieverts reaction conditions. The deeper hydrogenation pathway and reaction mechanism are currently under investigation and will be covered in a forthcoming study.

4 Conclusion

The combination of FTIR, XAS/XES, hydrogen uptake measurements and advanced modeling enables the identification of the species formed during the initial stages of the hydrogenation of MgB_2. FTIR, XAS and XES are consistent with one another and reveal the direct production of $Mg(BH_4)_2$ units from hydrogenation of MgB_2 under the modest pressure (145 bar) and at elevated temperatures (364–391 °C) used in the experiments. Moreover, no partially hydrogenated borane intermediates are observed under these conditions to within 0.5 mol% sensitivity. The persistence of the unoccupied $2p_{xy}$ state in B K-edge XAS, and the similarity in the XES spectra before and after initial hydrogenation point to a minimal number of B atoms being affected by the hydrogenation, which suggests full hydrogenation to BH_4^-. The FTIR confirms these results by directly identifying $Mg(BH_4)_2$ units in the hydrogenated product. The combined experimental and theoretical analyses point to a kinetic mechanism of initial hydrogenation described by hydrogen segregation at high-energy B–B bonds and ''etching'' of the boron from these edge binding sites inward. This mechanism is determined to consist of two steps, a H_2 dissociation step and a diffusive absorption step, by the simulations of hydrogen uptake curves using the devised kinetic model incorporating the relevant chemical reactions. Our results present a roadmap for integrating experiments and theory towards a more comprehensive understanding of complex reactions in solid-state hydrogen storage materials.

Acknowledgements

The authors acknowledge support from the Fuel Cell Technologies Office, Office of Energy Efficiency and Renewable Energy, of the U.S. Department of Energy (DOE) under Contracts DE-AC52-07NA27344 and DE-AC04-94AL85000. Thanks are extended to Marina Chong and Tom Autrey of Pacific Northwest National Lab for providing a sample of NaB_3H_8. John Vajo of HRL provided a sample of $BH_{0.36}$, which originated from the laboratory of Scott Anderson of U. Utah. The authors thank Dr David Prendergast and Dr Vincenzo Lordi for illuminating discussions on XAS/XES simulation as well as Dr Jinghua Guo and Dr Teak Boyko for outstanding assistance on beamlines 6.3.1.2 and 8.0.1.1 of the ALS and REIXS of the CLS, respectively. Portions of this research were performed at the ALS, Lawrence Berkeley National Laboratory, which is supported by the Director, Office of Science, Office of Basic Energy Sciences, of DOE under Contract DE-AC02-05CH11231. Portions of the research described in this paper were performed at the CLS, which is supported by the Canada Foundation for Innovation, Natural Sciences and Engineering Research Council of Canada, the University of Saskatchewan, the Government of Saskatchewan, Western Economic Diversification Canada, the National Research Council Canada, and the Canadian Institutes of Health Research. The authors thank Jane Manprasong for providing a nourishing environment for the conception of this collaborative work. The authors acknowledge helpful discussions through the Hydrogen Storage Materials Advanced Research Consortium (HyMARC) of the Fuel Cell Technologies Office of the DOE Office of Energy Efficiency and Renewable Energy. This work was performed under the auspices of DOE by Lawrence Livermore National Laboratory under Contract DE-AC52-07NA27344. Sandia National Laboratories is a multi-mission laboratory managed and operated by Sandia Corporation, a wholly owned subsidiary of Lockheed Martin Corporation, for the DOE's National Nuclear Security Administration under contract DE-AC04-94AL85000.

References

1 J. Keller, L. Klebanoff, S. Schoenung and M. Gillie, *Hydrogen storage technology: materials and applications*, CRC Press, Boca Raton, Florida, 2012, p. 3.
2 L. Klebanoff, J. Keller, M. Fronk and P. Scott, *Hydrogen storage technology: materials and applications*, CRC Press, Boca Raton, Florida, 2012, p. 31.
3 H.-W. Li, Y. Yan, S.-i. Orimo, A. Züttel and C. M. Jensen, *Energies*, 2011, **4**, 185–214.
4 L. Klebanoff and J. Keller, *Int. J. Hydrogen Energy*, 2013, **38**, 4533–4576.
5 J. M. Pasini, C. Corgnale, B. A. van Hassel, T. Motyka, S. Kumar and K. L. Simmons, *Int. J. Hydrogen Energy*, 2013, **38**, 9755–9765.
6 V. Konoplev and V. Bakulina, *Russ. Chem. Bull.*, 1971, **20**, 136–138.
7 Y. Nakamori, K. Miwa, A. Ninomiya, H. Li, N. Ohba, S.-i. Towata, A. Züttel and S.-i. Orimo, *Phys. Rev. B: Condens. Matter Mater. Phys.*, 2006, **74**, 045126.
8 K. Chłopek, C. Frommen, A. Léon, O. Zabara and M. Fichtner, *J. Mater. Chem.*, 2007, **17**, 3496–3503.
9 G. L. Soloveichik, Y. Gao, J. Rijssenbeek, M. Andrus, S. Kniajanski, R. C. Bowman, S.-J. Hwang and J.-C. Zhao, *Int. J. Hydrogen Energy*, 2009, **34**, 916–928.
10 V. Ozolins, E. Majzoub and C. Wolverton, *J. Am. Chem. Soc.*, 2008, **131**, 230–237.
11 H. Li, K. Miwa, N. Ohba, T. Fujita, T. Sato, Y. Yan, S. Towata, M. Chen and S. Orimo, *Nanotechnology*, 2009, **20**, 204013.
12 J. Yang, X. Zhang, J. Zheng, P. Song and X. Li, *Scr. Mater.*, 2011, **64**, 225–228.
13 M. Chong, A. Karkamkar, T. Autrey, S.-i. Orimo, S. Jalisatgi and C. M. Jensen, *Chem. Commun.*, 2011, **47**, 1330–1332.
14 M. Chong, M. Matsuo, S.-i. Orimo, T. Autrey and C. M. Jensen, *Inorg. Chem.*, 2015, **54**, 4120–4125.
15 O. Zavorotynska, S. Deledda and B. C. Hauback, *Int. J. Hydrogen Energy*, 2016, **41**, 9885–9892.
16 Y. Zhang, E. Majzoub, V. Ozoliņš and C. Wolverton, *J. Phys. Chem. C*, 2012, **116**, 10522–10528.
17 G. Severa, E. Rönnebro and C. M. Jensen, *Chem. Commun.*, 2010, **46**, 421–423.
18 C. Pistidda, S. Garroni, F. Dolci, E. G. Bardaj, A. Khandelwal, P. Nolis, M. Dornheim, R. Gosalawit, T. Jensen and Y. Cerenius, *J. Alloys Compd.*, 2010, **508**, 212–215.
19 R. J. Newhouse, V. Stavila, S.-J. Hwang, L. E. Klebanoff and J. Z. Zhang, *J. Phys. Chem. C*, 2010, **114**, 5224–5232.

20 H.-W. Li, T. Matsunaga, Y. Yan, H. Maekawa, M. Ishikiriyama and S.-i. Orimo, *J. Alloys Compd.*, 2010, **505**, 654–656.
21 P. Zanella, L. Crociani, N. Masciocchi and G. Giunchi, *Inorg. Chem.*, 2007, **46**, 9039–9041.
22 G. Kresse and J. Hafner, *Phys. Rev. B: Condens. Matter Mater. Phys.*, 1993, **47**, 558.
23 G. Kresse and J. Hafner, *Phys. Rev. B: Condens. Matter Mater. Phys.*, 1994, **49**, 14251.
24 G. Kresse and J. Furthmller, *Comput. Mater. Sci.*, 1996, **6**, 11169.
25 G. Kresse and D. Joubert, *Phys. Rev. B: Condens. Matter Mater. Phys.*, 1999, **50**, 1758.
26 J. P. Perdew and K. Burke, *Int. J. Quantum Chem.*, 1996, **57**, 309–319.
27 C. Massobrio, J. Du, M. Bernasconi and P. S. Salmon, *Molecular Dynamics Simulations of Disordered Materials*, Springer, 2015.
28 T. A. Callcott, L. Lin, G. Woods, G. Zhang, J. Thompson, M. Paranthaman and D. L. Ederer, *Phys. Rev. B: Condens. Matter Mater. Phys.*, 2001, **64**, 132504.
29 C. McGuinness, K. E. Smith, S. M. Butorin, J. H. Guo, J. Nordgren, T. Vogt, G. Schneider, J. Reilly, J. J. Tu, P. D. Johnson and D. K. Shuh, *EPL*, 2001, **56**, 112.
30 Y. Zhu, A. Moodenbaugh, G. Schneider, J. Davenport, T. Vogt, Q. Li, G. Gu, D. Fischer and J. Tafto, *Phys. Rev. Lett.*, 2002, **88**, 247002.
31 E. Kurmaev, I. Lyakhovskaya, J. Kortus, A. Moewes, N. Miyata, M. Demeter, M. Neumann, M. Yanagihara, M. Watanabe, T. Muranaka and J. Akimitsu, *Phys. Rev. B: Condens. Matter Mater. Phys.*, 2002, **65**, 134509.
32 C. Buzea and T. Yamashita, *Supercond. Sci. Technol.*, 2001, **14**, R115.
33 H. J. Choi, D. Roundy, H. Sun, M. L. Cohen and S. G. Louie, *Nature*, 2002, **418**, 758–760.
34 Y. Muramatsu, M. Oshima, T. Shoji and H. Kato, *Rev. Sci. Instrum.*, 1992, **63**, 5597–5601.
35 Y. Muramatsu, H. Takenaka, T. Oyama, T. Hayashi, M. M. Grush and R. C. Perera, *X-Ray Spectrom.*, 1999, **28**, 503–508.
36 Y. Wang, K. Michel and C. Wolverton, *Scr. Mater.*, 2016, **117**, 86–91.
37 M. H. Lee, M. J. Evans, L. L. Daemen, O. F. Sankey and U. Häussermann, *Inorg. Chem.*, 2008, **47**, 1496–1501.
38 M. H. Lee, O. F. Sankey, T. Björling, D. Moser, D. Noréus, S. F. Parker and U. Häussermann, *Inorg. Chem.*, 2007, **46**, 6987–6991.
39 Y. Wang, K. Michel, Y. Zhang and C. Wolverton, *Phys. Rev. B: Condens. Matter Mater. Phys.*, 2015, **91**, 155431.

